

Journal Pre-proof

ATP:Mg²⁺ shapes material properties of protein-RNA condensates and its partitioning of clients

N. Amy Yewdall, Alain A.M. André, Merlijn H.I. van Haren, Frank H.T. Nelissen, Aafke Jonker, Evan Spruijt

PII: S0006-3495(22)00685-3

DOI: <https://doi.org/10.1016/j.bpj.2022.08.025>

Reference: BPJ 11921

To appear in: *Biophysical Journal*

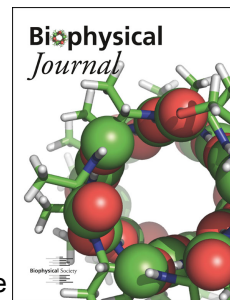
Received Date: 5 April 2022

Accepted Date: 19 August 2022

Please cite this article as: Yewdall NA, André AAM, van Haren MHI, Nelissen FHT, Jonker A, Spruijt E, ATP:Mg²⁺ shapes material properties of protein-RNA condensates and its partitioning of clients , *Biophysical Journal* (2022), doi: <https://doi.org/10.1016/j.bpj.2022.08.025>.

This is a PDF file of an article that has undergone enhancements after acceptance, such as the addition of a cover page and metadata, and formatting for readability, but it is not yet the definitive version of record. This version will undergo additional copyediting, typesetting and review before it is published in its final form, but we are providing this version to give early visibility of the article. Please note that, during the production process, errors may be discovered which could affect the content, and all legal disclaimers that apply to the journal pertain.

© 2022 Biophysical Society.



ATP:Mg²⁺ shapes material properties of protein-RNA condensates and its partitioning of clients

N. Amy Yewdall^{1*}, Alain A. M. André¹, Merlijn H. I. van Haren¹, Frank H.T. Nelissen¹, Aafke Jonker¹ and Evan Spruijt^{1*}

¹ Institute for Molecules and Materials, Radboud University, Heyendaalseweg 135, 6525 AJ, Nijmegen, the Netherlands

* Correspondence: e.spruijt@science.ru.nl, amy.yewdall@ru.nl

ABSTRACT

Many cellular condensates are heterotypic mixtures of proteins and RNA formed in complex environments. Magnesium ions (Mg²⁺) and ATP can impact RNA folding, and local intracellular levels of these factors can vary significantly. However, the effect of Mg²⁺:ATP on the material properties of protein-RNA condensates is largely unknown. Here, we use an *in vitro* condensate model of nucleoli, made from nucleophosmin 1 (NPM1) proteins and ribosomal RNA (rRNA), to study the effect of Mg²⁺:ATP. While NPM1 dynamics remains unchanged at increasing Mg²⁺ concentrations, the internal RNA dynamics dramatically slowed until a critical point, where gel-like states appeared, suggesting the RNA component alone forms a viscoelastic network that undergoes maturation driven by weak multivalent interactions. ATP reverses this arrest and liquefies the gel-like structures. Mg²⁺:ATP also influenced the NPM1-rRNA composition of condensates, and enhanced the partitioning of two clients: an arginine-rich peptide and a snoRNA. By contrast, larger ribosomes partitioning shows dependence on Mg²⁺:ATP, and can become reversibly trapped around NPM1-rRNA condensates. Lastly, we show that dissipative enzymatic reactions that deplete ATP can be used to control the shape, composition and function of condensates. Our results illustrate how intracellular environments may regulate the state and client partitioning of RNA-containing condensates.

SIGNIFICANCE STATEMENT

- Heterotypic condensates made from protein and RNA, such as the nucleolus, can exhibit puzzling gel-like morphologies that are at odds with fast protein dynamics that suggest liquid-like properties.
- Here, we highlight the importance of the RNA component.
- We show that the protein-RNA condensates are dynamic, adapting to local ATP concentrations through Mg²⁺-induced compaction of the RNA via enhanced RNA-RNA interactions, and reversible RNA relaxation when ATP binds Mg²⁺ again.
- With this, and our observation that the RNA component exhibits temperature-dependent aging, suggests the RNA component imparts viscoelastic properties onto protein-RNA condensates, driven by multivalent RNA-RNA interactions.
- In contrast, the protein component is free to diffuse throughout the RNA network.
- Other condensates containing RNA probably respond in similar ways to Mg²⁺ and ATP.

42 INTRODUCTION

43 Biomolecular condensates facilitate the spatiotemporal organization of cellular processes. Most biomolecular
44 condensates are heterotypic, and many arise from mixtures of proteins and nucleic acids, such as RNA (1).
45 Forming and existing in complex intracellular environments, the membraneless nature of condensates exposes
46 them to local environmental fluctuations. These fluctuating factors – ions, small molecules and temperature – can
47 all regulate the molecular interactions within condensates, which in turn, shapes their biophysical properties to
48 influence morphology and function (2,3). However, the intracellular parameter space of organisms is complex,
49 variable and not fully mapped. Therefore, *in vitro* studies can establish valuable insights into the influence of such
50 factors on condensate form and function.

51 It is well established that RNA structure is strongly influenced by magnesium ion (Mg^{2+}) concentrations (1,4,5),
52 which can range from 0.5-1 mM in eukaryotic cells and 1-5 mM in bacterial cell, as well as having an astounding
53 *in vivo* metabolite-bound concentration range of 20-100 mM (4,6). Indeed, the free Mg^{2+} concentrations can vary
54 throughout the cell cycle due to changes in levels of adenosine triphosphate (ATP), a nucleotide that strongly
55 complexes Mg^{2+} (5,7,8). Despite this, there has so far been no systematic analysis of the effect of Mg^{2+} and ATP
56 on shaping protein-RNA condensates.

57 With this, we are inspired by the nucleolus, a protein-RNA condensate that emerges during eukaryotic interphase
58 within a complex cellular environment. As the site of ribosome biogenesis, ribosomal RNA (rRNA) and various
59 RNA-binding proteins are predominantly found in this dynamic, but highly viscous, condensate. *In vivo* nucleoli
60 have slow fusion time scales of ~30 mins and non-spherical shapes (9-11), that are not well represented by *in*
61 *vitro* models, which are often liquid-like. Other heterotypic biomolecular condensates show similar divergent
62 dynamics between protein and RNA components (12). We hypothesize that RNA structuring and network
63 formation, governed by Mg^{2+} and other environmental factors, can partly explain these differences, and shape the
64 viscoelastic material properties of *in vitro* models of protein-RNA condensates.

65 In this work, we approximate part of the nucleolus by making model condensates from nucleophosmin 1 (NPM1)
66 protein and rRNA. By altering Mg^{2+} in the environment of model protein-RNA condensates, we shed light on how
67 this common divalent cation can dramatically slow RNA diffusion dynamics, until it arrests and non-spherical
68 condensate morphologies were observed. Additionally, NPM1-rRNA condensates underwent temperature-
69 dependent aging, particularly the rRNA component, which further supports the hypothesis that condensate
70 maturation is governed by multivalent RNA-RNA interactions, suggesting RNA's role in imparting viscoelastic
71 material properties to the condensate as a whole. The Mg^{2+} -stabilised arrested rRNA gel-like condensates were
72 liquefied using either temperature or ATP, with morphologies becoming increasingly spherical, and these changes
73 reflected in more fluid rRNA dynamics. We probed the functional consequence of different Mg^{2+} :ATP on NPM1-
74 rRNA condensates, and showed that these small molecules can impact client molecule partitioning. In particular,
75 we explored the intriguing formation of a 70S ribosome halo that transiently associated with the NPM1-rRNA
76 condensates. To allude to the intracellular enzymatic control of ATP levels, we used a dissipative enzymatic
77 reaction that depletes ATP, to regulate the biophysical properties of *in vitro* condensates and partitioning of
78 ribosomes. Together, our results not only provide a useful perspective for interpreting *in vivo* observations, but
79 also show that protein-RNA condensates are highly responsive to their environment, with the environment affecting
80 condensate properties, form and function.

81

82 MATERIAL AND METHODS

83 Reagents

84 Unless otherwise stated, all materials were obtained from Sigma-Aldrich.

85

86 Cloning of NPM1-wt into pET28a plasmid

87 The human nucleophosmin 1 gene was extracted from the pET28a(+)-NPM1-eGFP construct (gifted from R.K.)
88 and cloned into a pET28a(+) vector using *NdeI* and *XhoI* restriction sites. The correct insertion was confirmed by
89 sequencing (BaseClear, Leiden), and this construct called pET28a(+)-NPM1-wt.

90

91 NPM1 protein expression and purification

92 *E. coli* BL21 (DE3) were transformed with pET28a(+)-NPM1-wt. Overnight cultures were used to inoculate large
93 flasks of LB, then cells were grown at 37 °C to an $OD_{600} = 0.5-0.7$, before protein expression was induced with 1

mM IPTG. Protein expression was carried out at 20 °C for at least 16 hours, after which the cells were harvested by centrifugation. The pellet was resuspended in lysis buffer (20 mM Tris-HCl, pH 7.5, 300 mM NaCl, 2 mM β -mercaptoethanol, 25 mM imidazole) containing 500 U Bezonase® Nuclease and Bovine Pancreas RNase A (VWR). The resuspended cells were lysed using a homogenizer. Lysed samples were left at 4 °C for 1 hour to allow the enzymes to degrade the nucleic acids. The lysate was spun at 35000 $\times g$, 30 minutes at 4 °C in a Beckman JA25.50 rotor. The clarified supernatant was loaded onto a 5 mL HisTrapFF (Cytiva). After loading, the column was washed with 50 mL lysis buffer, and the His-tagged NPM1 proteins were eluted using elution buffer (20 mM Tris-HCl, pH 7.5, 300 mM NaCl, 2 mM β -mercaptoethanol, 250 mM imidazole). Eluted proteins were concentrated to <5 mL and loaded onto a Superdex 200 16/600 (GE Healthcare) size exclusion column connected to an AKTA Basic FPLC (GE Healthcare), and pre-equilibrated in storage buffer (20 mM Tris-HCl, pH 7.5, 300 mM NaCl). Fractionation of proteins was carried out at 1 mL/min, and monitored at 280 nm and 260 nm. The fractions of the main peak were pooled, and the protein concentration was determined using the NanoDrop One^C (Thermo Scientific). If the resulting UV spectrum had a 260/280 ratio of >0.6, the protein sample was further purified using anion exchange chromatography to remove contaminating nucleic acids. All protein isolates were dialyzed into storage buffer, aliquoted and snap frozen in liquid nitrogen and stored at -80 °C.

Protein labelling

The purified NPM1 proteins were labelled using AlexaFluor488 C₅ maleimide (ThermoFisher Scientific) based on a previously published protocol (13). Excess dye was removed using anion exchange, and the protein dialyzed into storage buffer. The final protein concentration was determined using the NanoDrop One^C. A labelled NPM1 stock was mixed with unlabelled protein at a 1:9 ratio of labelled:unlabelled protein, and this mixture was called NPM1-A488.

Sucrose gradient purified *E. coli* BL21 70S ribosomes were labelled using either ATTO488 NHS-ester (ATTO-TEC GmbH), or Dylight650 NHS-ester (ThermoFischer Scientific) dyes, as previously reported (14). The purified and labelled ribosomes were stored in aliquots at -80 °C until use. The final concentration of labelled 70S ribosome was estimated to be 5.1 μ M (A488 for ATTO488-labelled ribosomes) and 6.3 μ M (D650 for Dylight650-labelled ribosomes) determined using a Nanodrop 1000 (Isogen).

E. coli rRNA purification

E. coli BL21 cells were harvested from a 1 L culture in LB media ($A_{600} \sim 1.5$), and the cells were washed twice in buffer A (50 mM Tris, pH 7.7, 60 mM potassium glutamate, 14 mM magnesium glutamate, 2 mM DTT). Washed cells were lysed using the homogenizer, and insoluble debris was spun down at 20000 $\times g$ for 25 minutes. The supernatant containing the ribosomes was removed and the ribosomes were pelleted by centrifugation for 3 hours at 50000 rpm at 4 °C in a Beckman Ti70.1 rotor. The pellet containing the ribosomes was resuspended in buffer A, and the rRNA was purified using standard phenol-chloroform extraction protocols. The final rRNA concentration was determined using the Nanodrop One^C, where 1 OD₂₆₀ = 40 μ g/mL RNA.

RNA labelling using periodate oxidation

The 3'-hydroxyl of RNA was labelled with AlexaFluor™647-hydrazide (ThermoFisher Scientific) using periodate oxidation based on manufacturer's protocol. The RNAs labelled using this procedure included the purified rRNA, polyadenylic acid potassium salt (P9403 Sigma) or polyuridylic acid potassium salt (P9528 Sigma). The nucleic acids were purified using a standard isopropanol precipitation followed by 70% ethanol precipitation, or using the Amicon®-Ultra spin concentrators (Millipore) (as per method described (15)). An agarose gel was used to double check complete free dye removal, before the sample concentrations were calculated using the Nanodrop One^C, where 1 OD₂₆₀ = 40 μ g/mL RNA, and the dye fluorescence concentration was calculated using the extinction coefficient (at 649 nm) of 250,000 $\text{cm}^{-1}\text{M}^{-1}$ (as described by the manufacturer). The AlexaFluor647-labelled RNAs were denoted with A647.

Making NPM1-RNA condensates

All experiments were performed using a standard base buffer (20 mM Tris-HCl, pH 7.2, 250 mM potassium glutamate) with different concentrations of magnesium glutamate (often denoted as Mg²⁺), as specified per experiment. The buffers were made as a 4X concentrated stock and were diluted to a final 1X working concentration, along with the other components, using Milli-Q water. The final concentrations of NPM1 protein and RNA used in every experiment were 20 μ M and 100 ng/ μ L, respectively. Under all buffer conditions, NPM1 was required to nucleate NPM1-RNA condensate formation. In a typical experiment, the 4X buffer is first mixed with Milli-Q water, followed by RNA, then the NPM1, after which samples were mixed and pipetted onto a functionalized

150 microscopy slide for imaging. Unless otherwise stated, samples were left to incubate on the glass slides at room
 151 temperature for at least 45 minutes before imaging.
 152

153 **Fluorescence confocal microscopy setups**

154 Two fluorescence confocal microscopy setups were used for the experiments in this paper: (1) Olympus IX81
 155 spinning disk confocal microscope, equipped with an Andor FRAPPA photobleach module and Yokogawa CSU-
 156 X1 spinning disk. The Andor 400 series solid state lasers were used to bleach and image the samples. All the
 157 images were recorded with a 100× oil immersion objective (NA 1.5) and an Andor iXon3 EM CCD camera. (2)
 158 Leica SP8 Liachroic-beam splitting confocal laser scanning microscope, equipped with a PMT detector, 2 x HyD
 159 SP GaAsP detectors and Leica DRC7000 GT monochrome camera. All the images recorded using this confocal
 160 used a HC PL APO 63x/1.40 (oil) CS2 (0.14 mm) objective.

161 Two types of microscopy slides were used: the 18-well Ibidi chambers for quick imaging, as well as PDMS
 162 chambers made in-house. The PDMS chambers were attached onto plasma-primed cover glass slides (No. 1.5H).
 163 These PDMS chambers were used for experiments that exceeded 1 hour, as Vaseline-sealed coverslips were
 164 applied on top to avoid evaporation. For both setups, the glass surfaces were cleaned using a plasma cleaner,
 165 then incubated for 1 hour with 0.1 mg/mL PLL(2)-g[3.5]-PEG(2) (SuSoS AG, Switzerland) dissolved 10 mM
 166 HEPES, pH 8.0, before the surface was thoroughly washed with Milli-Q water and dried with nitrogen gas.
 167

168 **Fluorescence recovery after photobleaching (FRAP)**

169 Fluorescence recovery after photobleaching (FRAP) experiments were conducted on the Olympus IX81 spinning
 170 disk confocal microscope set-up. FRAP measurements were carried out by selecting a small ROI in the middle of
 171 a coacervate or aggregate of interest, and bleaching with the appropriate wavelength of the laser, depending on
 172 the sample. The 488 nm laser line was set at 100% laser power using 75 pulses of 150 μs, and the 647 nm laser
 173 line was set to at 100% laser power using 75 pulses of 100 μs. When both wavelengths were used, the 647 nm
 174 laser bleaching preceded that of 488 nm laser. The recovery was imaged at reduced laser intensity (at least 5-
 175 fold lower) and a regular time intervals, depending on the sample.

176 Using a MATLAB script, the experimental recovery was first normalized before being fitted to a simple
 177 exponential, as a first-order approximation of 2D diffusion with a fixed boundary (i.e. droplet edge) (16). Briefly,
 178 the exponential decay equation: $y = A(1 - e^{-bt}) + C$

179 From this equation, the recovery half-life (τ) was calculated by $\tau = \ln(2) / b$ and percentage recoveries
 180 were extracted by multiplying A by 100. We note that the theoretical maximum recovery is limited by the size of
 181 the bleached spot, which was $13.1 \pm 4.4\%$ of the droplet area in our experiments, corresponding to a maximum
 182 theoretical recovery of ~87%.
 183

184 **Aging experiments**

185 The CSU temperature stage (Tokai-HIT) was used to set the temperature of the samples within a range of 8 –
 186 39 °C. Sample temperatures were always confirmed using a thermometer at the end of each experiment. The
 187 condensate components and buffers were pre-incubated at the temperature of interest prior to mixing, and being
 188 immediately added to functionalized PMDS slides that were sealed with Vaseline. An Arrhenius plot of the τ data
 189 revealed two straight lines with a transition around 21-22 °C (**Figure S2A**) and a transistivity plot (**Figure S2B**) was
 190 derived from the Arrhenius plot to show this drastic transition.
 191

192 **Circularity (Figures 2C and D)**

193 The NPM1-rRNA condensates were mixed and deposited onto the Vaseline-sealed PDMS slides incubating at
 194 8 °C (sample temperature). Note the CSU temperature (Tokai-HIT) stage was set to 4 °C, but sample temperature
 195 was recorded throughout the experiment using a buffer blank in an adjacent well, and it is the sample temperature
 196 that is reported in our figures. Samples were incubated for at least 45 mins before imaging began. Sample
 197 temperature was adjusted incrementally with a 10-minute pause before imaging. At least three different images
 198 were captured and the circularities calculated here were averaged across the population of condensates.

199 To monitor changes to the condensate circularity upon ATP addition, the NPM1-rRNA condensates were
 200 made in 14 mM Mg²⁺ buffer and left to incubate in Ibidi slides for 50 minutes before 11 mM ATP was added to a
 201 corner of the slide. Using the Olympus IX81 confocal microscope, the sample with focus on one large condensate
 202 was imaged and the circularities calculated over time. We expect the circularity for the single condensate after
 203 ATP addition to be less than 1 because the final free Mg²⁺ concentration was 3 mM. Indeed, the circularity of the
 204 sample population was to 0.85 ± 0.13 after ATP addition.

205 Raw fluorescence confocal microscopy images and videos were processed and analysed with MATLAB
 206 2021 Image Processing Toolbox. Objects smaller than 200 pixels were excluded from the analysis (to avoid
 207 detecting smaller spherical droplets that tend to initially form as they settle onto the glass) and the area and mean

intensity were extracted for every object in each frame. For circularity calculations, the perimeter of each object was calculated by taking the sum of all pixels that were directly adjacent to the dilute phase plus half the sum of all pixels that were only diagonally adjacent to the dilute phase. The circularity (ϑ) of the object cross section was then calculated as $\vartheta = 4\pi A/P^2$, where A is the area of the object and P the perimeter (17). Subsequently, a single ϑ for each frame was calculated by taking the mean $\vartheta \pm$ standard deviation.

ATP, ADP and AMP experiments (Figure 2 E-G)

Samples were prepared in a sequence as outlined above, and nucleotides were mixed last before everything was deposited onto a glass slide for imaging. The samples were mixed in base buffer containing 14 mM Mg^{2+} , and each nucleotide was at 10 mM final concentration. The FRAP experiments were performed as outlined above. Errors are standard deviations from at least duplicate experiments.

SYBR Gold intensity calculations (Figure S6)

SYBR Gold was used to indirectly probe rRNA compaction within the condensates. According to Kolbeck *et al*, the SYBR Gold 10000X stock is 12.4 ± 1.2 mM. Therefore, at 40 nM, the final SYBR Gold concentration used per 30 μ L experiment is 62.5X below that of the reported 2.5 μ M concentration where quenching effects were observed. SYBR Gold fluorescence is dependent on not just concentration, but also local environment (18). To test this, the condensate samples – using unlabelled components – were pre-mixed as outlined above and the SYBR Gold was added last. In some cases, the Mg^{2+} and ATP were added sequentially after condensate formation. There were no noticeable differences in fluorescence when comparing with pre-mixed and sequential samples. In fact, our reported results are a combination of sequential and pre-mixed intensities.

Since we were comparing SYBR Gold fluorescence between samples with different Mg^{2+} and/or ATP concentrations, the confocal images were taken using the Leica SP8 set-up. For all the images, the same laser settings were used. The fluorescence intensity of SYBR Gold from confocal microscopy images and videos were processed and analysed with MATLAB 2021 Image Processing Toolbox. The images were binarized with an automatic intensity threshold computed with Otsu's method (19). Objects smaller than 50 pixels were excluded from the analysis and the area and mean intensity were extracted for every object in each frame.

Partitioning experiments (Figure 3 A-C)

For partitioning of client molecules we prepared stock solutions at 33 μ M 5,6-FAM-RP3 (CASLO) and 50 μ M 5,6-FAM-SNORD52 (IDT) in the standard base buffer containing 5 mM Mg^{2+} . The ribosome clients, 70S ribosomes-A488 and 70S ribosomes-D650, were thawed and centrifuged for 10 minutes at 20000 xg to remove any aggregates, and the supernatant was used for partitioning experiments. The ribosome concentration in the supernatants did not diverge much from the stock concentrations described above.

For each partitioning experiment, 1 μ L client was mixed with either the forming coacervates, or with the RNA component prior to NPM1 addition. Both orders of addition yielded similar results. The mixtures were incubated for 45 minutes on the glass slides at room temperature, before imaging.

For imaging, we used the Leica confocal setup with laser excitations of 488 nm (FAM, ATTO488) and 647 nm (Dylight650). For each laser setting, a blank was imaged made from NPM1-rRNA with one of the components labelled, accordingly. The partitioning coefficient was then calculated using: $K_p = (I_{coacervate} - I_{background}) / (I_{dilute} - I_{background})$, where $I_{coacervate}$ is the average intensity as determined by a pixel gray value cut off above 40, and I_{dilute} is the average intensity as determined by a pixel gray value cut-off below 10. The errors are standard deviations of at least three sets of K_p values derived from three different images.

Ribosome halo formation

The ribosome halo formation was monitored over time using both confocal set-ups as highlighted in the video captions. The pixel intensity measurement (Figure 3F) was from a time-lapse experiment of ATTO488-labelled 70S ribosomes where the video was taken shortly after sample mixing. Using ImageJ, a line of fixed pixel length (equivalent to 9.23 μ m) was drawn and the pixel intensity for each frame of the droplet was measured.

Apyrase enzyme experiments (Figure 6)

Apyrase Grade VII from Potato enzyme was dissolved in standard base buffer containing 5 mM Mg^{2+} (20 mM Tris-HCl, pH 7.2, 250 mM potassium glutamate, 5 mM magnesium glutamate). For the FRAP experiment, the samples were made using 5 mM Mg^{2+} base buffer with additives: ATP, AMP and ATP with apyrase. 5 U apyrase solution was added to the forming coacervate mix and all the samples were left to equilibrate on the Ibi microscope slides for 30 minutes before imaging and FRAP experiments were performed. Error bars are standard deviations from at least two different photobleaching experiments.

265 The morphology changes to the NPM1-rRNA condensates were monitored using the Leica SP8 confocal
266 microscope. Again, the samples were prepared as above, with 5U apyrase added to the forming coacervates. The
267 sample was left to incubate on functionalized Ibidi slides for 30 minutes prior to imaging using both the 488 nm
268 (NPM1-A488) and 647 nm (rRNA-A647).

269 Lastly, for the ribosome halo and apyrase experiments, 5 U apyrase solution was added to the formed
270 coacervates on one side of the well of the microscope slide, and the disappearance of the ribosome halo was
271 monitored every 1 second.

Journal Pre-proof

272 **RESULTS**

273

274 **Mg²⁺-induced RNA compaction slows dynamics and leads to gelation**

275 In order to probe the influence of environmental factors on heterotypic condensates that contain both RNA and
 276 protein components, we chose NPM1-rRNA as a model system (**Figure 1A**). NPM1 proteins are localized to the
 277 outer layer of the nucleoli, in the so-called granular component, and was shown to readily form condensates with
 278 rRNA *in vitro* (10). Similar to previous work (10), by mixing NPM1 proteins with rRNA in buffer containing no Mg²⁺,
 279 spherical liquid-like droplets appeared. Simultaneous fluorescence after photobleaching (FRAP) analyses for both
 280 protein and RNA components demonstrated a noticeable difference in FRAP recovery even at 0 mM Mg²⁺
 281 concentration, with a faster recovery half-life (τ) for NPM1 at 18.3 ± 2.4 s and slower recovery for rRNA at $30.7 \pm$
 282 6.1 s (**Figure 1B and C**). The τ for NPM1 is comparable to *in vivo* values of around 20 s (10,20). The difference
 283 between protein and RNA recoveries is reminiscent of other intracellular protein-RNA condensates, where the
 284 constituent RNAs recover slower than protein components; this was attributed to multivalent RNA-RNA
 285 interactions (12,21).

286 In order to promote such RNA-RNA interactions in the NPM1-rRNA condensates, we increased the Mg²⁺
 287 concentrations and checked the partitioning of each of the components within the condensates (**Figure 1D**). At
 288 higher Mg²⁺, rRNA partitions more strongly within condensates. We also observed the NPM1 protein and RNA
 289 dynamics diverge, with rRNA recovering slower and to a lesser extent (**Figure 1E and F**), while NPM1 recovery
 290 remained unchanged. At Mg²⁺ concentrations higher than 7 mM, rRNA is fully arrested with $\tau > 1500$ s and
 291 percentage recoveries decreased to $< 10\%$ (**Figure 1G**). These findings suggest a gradual transition from liquid to
 292 an arrested, gel state of the RNA component of the nucleolus, which is supported by the scaling behavior of the
 293 relaxation times near the critical point (**Figure 1E**) (22,23). The NPM1 component remained astonishingly mobile
 294 within the rRNA gel network as the Mg²⁺ concentration increased, with low τ (**Figure 1E**), which is consistent with
 295 other reported FRAP recoveries for proteins in tangled RNA networks (10,20). The percentage recovery of NPM1
 296 proteins appeared to not significantly decrease until 20 mM Mg²⁺ was reached (**Figure 1F**). NPM1 thus shuttles
 297 between different regions of the gelled RNA network. Finally, we note that when rRNA dynamics is fully arrested,
 298 the condensates adopt an irregular-shaped morphology (**Figure 1G**) with gel-like states that can still slowly fuse
 299 together within the time scale of several minutes (**Video S1**), reminiscent of nucleoli fusing *in vivo* (9). These
 300 results suggest that RNA-RNA interactions, and by extension, Mg²⁺ concentrations, play an important role in
 301 shaping condensate dynamics.

302 Mg²⁺ stabilization of RNA-RNA interactions and corresponding compaction of RNA chains is well reported (1,4,5).
 303 The observed rRNA arrest at high Mg²⁺ is likely due to the compaction of RNA, promoted by enhanced RNA-RNA
 304 base-pairing and stacking interactions, leading to slowed diffusion of these entangled polymers in the dense phase.
 305 To further explore this process, NPM1 condensates were made with other homopolymeric RNAs with different
 306 propensities for RNA-RNA interactions. Poly-adenosine (pA) RNA is known to form base-stacking interactions with
 307 Mg²⁺, whereas poly-uridine (pU) remains largely unstructured (24). At 20 mM Mg²⁺, condensates made from rRNA
 308 or pA both formed gels, whereas condensates made from pU remained spherical, liquid droplets (**Figure 1H**) that
 309 still readily fused with one another within seconds (**Video S2**). The FRAP parameters also reflected this, with τ
 310 increasing for pA at increasing Mg²⁺, but pU τ 's were unaffected by Mg²⁺ (**Figure 1I**). The gelation induced by RNA
 311 compaction can also be seen in decreasing percentage recoveries for pA at increasing Mg²⁺ concentrations, while
 312 pU percentages remained relatively unchanged (**Figure 1J**), in agreement with previous studies on Mg²⁺-induced
 313 folding of single 16S rRNA and pU mRNA molecules (25). Together, these results suggest that RNA compaction
 314 is facilitated by Mg²⁺ induced RNA-RNA interactions, which occur in RNAs with strong base pairing and base
 315 stacking interactions, such as rRNA and pA, but not in RNAs with weak base stacking interactions, such as pU.
 316 Together, our results suggest that, in systems where RNA-RNA interactions can be stabilized with Mg²⁺, the RNA
 317 component imbues protein-RNA condensates with viscoelastic material properties.

318

319 **Tuning rRNA compaction with temperature and ATP**

320 We hypothesize that RNA forms a viscoelastic network in heterotypic protein-RNA condensates, such as for this
 321 NPM1-rRNA system, based indirectly on the partial FRAP recoveries and slowing dynamics with increasing Mg²⁺.
 322 Additional evidence for the viscoelastic nature of the rRNA component is its gradual aging to a more structured
 323 state, with slower relaxation observed as an increasing τ over time that reaches a plateau (**Figure 2A**). In contrast,

324 the τ of NPM1 remains relatively constant over time (**Figures 2B and S1**). This relaxation varies non-linearly with
 325 the inverse temperature ($1/T$), which further supports the viscoelastic nature of rRNA in the condensates. In a pure
 326 viscous liquid, where FRAP recovery is commonly attributed to simple Stokes-Einstein diffusion, the diffusion
 327 coefficient should increase as $1/T$, and the recovery time should be linearly proportional to temperature. However,
 328 this is clearly not the case for NPM1/rRNA condensates, as there is a strong non-linear dependence of τ on T
 329 (**Figure 2B**). A closer inspection reveals that the temperature dependence shows signs of an activated process
 330 that leads to structuring and relaxation. Our data can be fitted using an Arrhenius equation with a fixed activation
 331 energy for temperatures above the gel point (**Figure S2A**). Below that point, the activation energy increases to a
 332 higher level, as shown by the transitivity plot (**Figure S2B**), which is characteristic of gels and glasses (26).
 333 Therefore, even at 0 mM Mg^{2+} , the rRNA network appears to be a viscoelastic material, held together by multivalent
 334 intra- and intermolecular RNA-RNA interactions. In contrast, the NPM1 protein can diffuse freely under all
 335 conditions, consistent with observations that nucleoplasmic NPM1 concentrations increase with higher overall
 336 NPM1 expression levels (27).

337 Since Mg^{2+} stabilizes RNA-RNA interactions, it was anticipated that this could affect the τ at maturation of
 338 condensates formed in Mg^{2+} buffer. Indeed, condensates made in 5 mM Mg^{2+} had slower observed τ at maturation,
 339 which decreased at higher temperature (**Figure S3**). This result made us curious about the effect of temperature
 340 on Mg^{2+} -stabilized RNA-RNA interactions, and how this could impact condensate morphology. NPM1-rRNA
 341 condensates formed at 8 °C, in either 5 mM or 10 mM Mg^{2+} buffer after 60 minutes of incubation, had a striking
 342 non-spherical morphology (**Figures 2C and S4**). The 10 mM Mg^{2+} condensates appeared smaller and had lower
 343 average circularity than the 5 mM Mg^{2+} condensates, but both circularities were lower than at higher temperatures,
 344 where values increased closer to 1, which is a characteristic of spherical liquid droplets(17). These results suggest
 345 that RNA is fully arrested at lower temperatures in 10 mM Mg^{2+} , with the small gel-like condensates unable to
 346 completely fuse together. Instead, the small gel droplets partially fuse, at the time of formation, to form irregular-
 347 shaped condensates similar to other gel-like RNA condensates (12). As temperature was increased, the gel-like
 348 condensates relaxed and coalesced, eventually, into spherical droplets, which resulted in increased average
 349 circularity of the condensate population (**Figure 2C**). In fact, the condensates appeared spherical at 35 °C, with
 350 circularities close to 1, for both Mg^{2+} concentrations. This temperature-dependent relaxation of the NPM1-rRNA
 351 condensates manifesting as a morphological change provides further evidence for gelled states being caused by
 352 RNA compaction that results in incomplete fusion of gel condensates. Since circularity changes are a one-way
 353 process, we demonstrated thermo-reversibility of the rRNA component in condensates using FRAP (**Figure S5**).
 354 The responsive morphology changes of NPM1-condensates within the temperature range of living systems, hints
 355 that this could be an important parameter to consider for nucleoli dynamics.

356 In homeostatic eukaryotic cells, Mg^{2+} concentrations and temperature are often well regulated (28,29), but local
 357 ATP levels are known to fluctuate (7,8). ATP strongly chelates Mg^{2+} , changing the effective free Mg^{2+}
 358 concentrations. When we tested the effect of ATP addition to the NPM1-rRNA condensates that were incubated
 359 with Mg^{2+} , we observed that ATP caused the gel-like morphologies to liquefy, and the circularity increased over
 360 20 minutes (**Figure 2D**). ATP relaxes the rRNA network, with FRAP recoveries corresponding to the remaining
 361 free Mg^{2+} concentrations (**Figure S6**). In order to probe the influence of ATP on RNA compaction, we used SYBR
 362 Gold fluorescence to probe the RNA-RNA interactions within the condensates. SYBR Gold is a fluorescent dye
 363 that intercalates double stranded nucleic acids (18), and we hypothesize that Mg^{2+} will stabilize such interactions
 364 between the rRNAs. This was indeed the case, as the average SYBR Gold fluorescence detected inside the
 365 NPM1-rRNA condensates increased by ~41% on Mg^{2+} addition (**Figure S7**). Subsequently, the SYBR Gold
 366 fluorescence decreased when ATP was added, providing indirect evidence for decreased RNA compaction due
 367 to ATP chelating Mg^{2+} (**Figure S7**). This liquefying effect is less pronounced for other adenosine nucleotides (ADP
 368 and AMP) that do not chelate Mg^{2+} as effectively (**Figure 2E-G**). These results demonstrate how ATP can be a
 369 key regulator of free Mg^{2+} concentrations that can impact NPM1-rRNA condensate dynamics.

370 371 **Consequences of ATP: Mg^{2+} on condensate function: partitioning of clients**

372 Alongside chelating Mg^{2+} , ATP can also bind to the nucleic acid interacting domain of NPM1 (30,31), which could
 373 lead to an altered chemical microenvironment inside the condensates. Inspired by the profound changes to
 374 condensate dynamics observed with Mg^{2+} and ATP, we were curious whether these small molecules would
 375 influence the partitioning of component proteins, RNAs and client molecules inside the condensates. Indeed, we
 376 observed that, at higher Mg^{2+} when there is no ATP, the partitioning coefficient (K_p) of rRNA increased on
 377 compaction, and the NPM1 protein K_p decreased, as more RNA-RNA interactions could exclude protein-RNA

378 interactions (**Figure 3A and B**). ATP increased the K_p of both RNA and protein components. We speculate that
 379 ATP, when bound to the nucleic acid interacting domain (30,31), can also stabilize the interaction between NPM1-
 380 rRNA, because the nucleic acid interacting domain is also where NPM1 binds rRNA (32). As a result, a synergistic
 381 increase in partitioning of both components inside the condensates occurred only when Mg^{2+} and ATP were
 382 present, and not when ADP or AMP were present (**Figure S8**).

383 We then tested whether the altered microenvironment has a functional consequence in the partitioning of two
 384 model clients, the (RRASL)₃ peptide (RP3) and the SNORD52 RNA. RP3 resembles arginine-rich peptides that
 385 can electrostatically interact with both the NPM1 protein and rRNA (33), whereas SNORD52 is a small nucleolar
 386 RNA that binds specifically to NPM1 (34) (**Figure 3C**). The K_p of both clients followed trends that are expected
 387 based on their interaction strengths with the condensate components (**Figure 3C**). The SNORD52 RNA K_p
 388 increased at higher ATP concentrations as more NPM1 partitioned into the condensates. Conversely, the RP3 K_p
 389 decreased as less binding surface was expected due to the synergistic partitioning and interaction of NPM1 and
 390 rRNA at higher ATP concentrations. These results indicate that Mg^{2+} :ATP can be used to tune client partitioning
 391 within NPM1-rRNA condensates.

392 As nucleoli are the sites of ribosome biogenesis, we next investigated the effect of Mg^{2+} and ATP on the partitioning
 393 of ribosomes into NPM1-rRNA condensates. Here, we used labelled mature 70S ribosomes that should remain
 394 intact at Mg^{2+} concentrations above 5 mM (6). Therefore, it is unsurprising that at increasing Mg^{2+} , the K_p
 395 decreased as the ribosomes remained intact in solution (**Figure S9**). In contrast, ATP addition resulted in a 30%
 396 increase in K_p , likely due to chelation of Mg^{2+} that was previously bound to the ribosomes, thereby destabilizing
 397 the ribosome structure and causing it to partition inside the NPM1-rRNA condensate (**Figure S9**). This
 398 destabilization of ribosome structure was previously reported when free Mg^{2+} concentrations were below 5 mM
 399 (35). Interestingly, under conditions where Mg^{2+} concentrations exceeded ATP concentrations, the ribosomes
 400 formed a striking halo around the NPM1-rRNA condensates (**Figures 3D and E**). The ribosome halo excluded the
 401 rRNA, and resulted in a deformed rRNA condensate shape (**Figure 3D**). In contrast, the NPM1 fluorescence is
 402 homogeneously distributed throughout the condensates localizing to both the ribosome and rRNA (**Figure 3E**),
 403 which is expected from a protein that can bind to all rRNAs present. Indeed, these heterotypic multicomponent
 404 interactions of NPM1 with rRNA and the pre-ribosomal subunits, have been suggested to drive ribosome assembly
 405 (27), and here we show that NPM1 bridges the interactions between the rRNA component within the condensates
 406 and the 70S ribosomes in the halo.

407 In order to examine our hypothesis that the halo appeared due to partly destabilized 70S ribosomes, we monitored
 408 the condensate growth over time. The ribosome halo appeared after ~25 minutes, with an increased fluorescence
 409 intensity observed around the edge of the condensates (**Figure 3F**). Here, the ribosome-NPM1-rRNA condensates
 410 exhibited decelerated fusion between larger droplets, in the order of tens of minutes (**Video S3**). A possible reason
 411 for slow droplet fusion could be the viscoelastic nature of the ribosome halo and its rearrangement that would be
 412 necessary for rRNA-NPM1 condensates to fuse. Indeed, we found that the ribosome halo had slow FRAP
 413 dynamics with an average τ of 490 ± 10 s, and percentage recoveries of $45 \pm 11\%$. As the droplets fused, the
 414 ribosome halo seemed to become incorporated into the condensate and appeared inside as bright spots, with
 415 some droplets stalled mid-fusion (**Video S3**). As a control, we made NPM1-rRNA condensates in 10 mM Mg^{2+} and
 416 left these to mature for 2 hours, before 5 mM ATP was added, to verify that the observed halo was not a transient
 417 phenomenon linked to nucleoli maturation, but rather a result of destabilized ribosomes that originate from the
 418 dilute phase. Here, the ribosome halo also appeared after approximately ~10 minutes of ATP addition, alongside
 419 separate droplets composed of NPM1 and ribosomes (**Video S4, Figure S10**), which is reminiscent of *in vivo*
 420 experiments showing NPM1 interacting with 60S pre-ribosomes (36). Our results suggest that the ATP addition
 421 destabilizes the ribosomes in solution, which in turn could liberate ribosome-associated rRNA to interact with
 422 NPM1, forming the halo. The exclusion of partially destabilized ribosomes from the NPM1-rRNA condensates is
 423 an exciting result as this corroborates the *in vivo* behavior of nucleoli (27), but to our knowledge this is the first
 424 time this phenomenon has been observed *in vitro*. Therefore this work not only provides a useful platform for
 425 further studying thermodynamic exclusion from condensates, but also suggests that ATP: Mg^{2+} could be one of the
 426 ways cells can alter the condensate environment to drive ribosome formation.

427

428 Enzymatic depletion of ATP levels changes condensate properties and function

429 Within cells, ATP levels fluctuate due to a variety of enzymes: from ATP-dependent chaperones to reactions that
 430 consume ATP (5,7,8). Here we demonstrate that ATP removal using a dissipative enzymatic reaction can also

431 control the condensate properties of the nucleolus-like condensates made from NPM1 and rRNA. Using apyrase,
432 an enzyme that converts ATP to AMP (**Figure 4A**), we showed that the rRNA recovery of samples without and
433 with apyrase reflected those for the ATP and AMP nucleotides, respectively, similar to observations in Figure 2
434 (**Figure 4B-D**). Apyrase can effectively liberate Mg^{2+} from ATP, thereby causing rRNA arrest and morphology
435 changes for samples made in high Mg^{2+} concentrations (**Figure 4E-G**). This change in morphology from spherical
436 liquid-like to irregular-shaped gel-like states is remarkably similar to observations for purified and *in vivo* nucleoli
437 when ATP was depleted (9,11). For the purified and *in vivo* nucleoli, ATP-dependent chaperones were
438 hypothesized to facilitate liquid-like condensate dynamics. However, our results highlight the impact of liberated
439 Mg^{2+} due to ATP depletion, and demonstrate that changes to free Mg^{2+} levels may corroborate these *in vivo* and
440 our *in vitro* observations. Here, enzymes that consume ATP, and not necessarily active ATP-dependent
441 chaperones, are a possible route that cells use to regulate Mg^{2+} levels and impact nucleoli dynamics.

442 As nucleoli should exclude fully folded ribosomes (27), we were curious whether ATP removal would affect the
443 previously observed ribosome halo around the NPM1-rRNA condensates. We hypothesized that the ribosome
444 halo was formed from destabilized ribosomes interacting with NPM1, but to what extent the ribosomes were
445 destabilized and whether this was reversible was not yet clear. ATP was depleted using apyrase, which resulted
446 in increased available Mg^{2+} concentrations, and as a result, we observed the striking disappearance of the
447 ribosome halo over time (**Figure 4H**). Additionally, the ribosome-NPM1 puncta formed outside the NPM1-rRNA
448 condensates (**Video S5**) also vanished on apyrase addition, suggesting that fully folded ribosomes are excluded
449 from the NPM1-rRNA condensates. With the disappearance of the ribosome halo, the NPM1-rRNA condensates
450 that were previously stabilized mid-fusion were able to relax and fuse again, and the resulting condensates
451 appeared unexpectedly spherical in shape (**Video S6**), despite the higher available Mg^{2+} concentrations. The more
452 spherical final condensates are hypothesized to be a result of altered Mg^{2+} ions concentrations: although liberated
453 from ATP, the Mg^{2+} will likely bind to the 70S ribosomes making the ion less available to stabilize rRNA-rRNA
454 interactions. These results demonstrate that enzymatic changes to ATP concentrations can have a profound effect
455 on client localization around the NPM1-rRNA condensates, and could indeed be a way how cells change the flux
456 of client molecules interacting with nucleoli.

457

458 DISCUSSION

459 Many biomolecular condensates are portrayed as heterotypic protein-RNA droplets with viscoelastic material
460 properties, governed by primarily by interactions between proteins and RNA (2,3,37,38). However, here we show
461 that the RNA component itself has a determining role in the shape, dynamics and material properties of protein-
462 RNA condensates, especially in systems where the RNA network is formed via RNA-RNA interactions tuneable
463 by changes in Mg^{2+} -ATP, or temperature. The viscoelastic properties of the RNA network depend on the structure
464 of the RNA and the strengths of the intermolecular RNA-RNA interactions. NPM1-pU condensates, for example,
465 remained largely liquid-like even at high Mg^{2+} , suggesting pU RNAs do not form a strong network, while NPM1-
466 rRNA and NPM1-pA condensates showed dynamic arrest at high Mg^{2+} . Indeed, our results at high Mg^{2+} for rRNA
467 and pA condensates are reminiscent of the gel-like morphologies observed in reconstituted protein-RNA
468 condensates, where increased intermolecular interactions are engineered for one component, either protein (39)
469 or RNA (12,24), within the network. Here, we demonstrate that also the environment can influence the
470 intermolecular interactions in RNA, and this can be a way to control the dynamic material properties of protein-
471 RNA condensates, like NPM1-rRNA condensates.

472 Homotypic protein-based condensates were previously shown to mature over time as viscoelastic Maxwell fluids
473 (40), with slowed aging at increased temperatures. The aging of NPM1-rRNA condensates is similarly
474 temperature-dependent with faster τ at maturation for RNA at higher temperatures. This plateau in τ observed after
475 1h is also reminiscent to another *in vitro* system of protein-only condensates formed via Ni^{2+} interactions (41).
476 Additionally, an aging phenomenon was also documented for *in vivo* protein-RNA condensates where FRAP
477 recoveries of the protein component at 5 hours after formation was faster than at 16 hours (12). Although the
478 physiological relevance is still unknown, aging seems to be a common feature of viscoelastic condensates formed
479 via multivalent interactions, and here, we show for the first time, that the RNA component also undergoes aging.

480 Since nucleoli are rich in RNA (42), our work on NPM1-rRNA condensates, highlighting the considerable influence
481 of Mg^{2+} -ATP on the dynamics of the RNA network, can in turn help us better interpret the puzzling observations of
482 actual nucleoli. Indeed, *in vivo* nucleoli are gel-like, with slow fusion time scales of ~30 minutes and non-spherical
483 shapes (9-11), however the localised proteins had fast dynamics, in the order of seconds (20,43), which never

484 explained the material properties of nucleoli. By considering the RNA component, our work shows that NPM1-
 485 rRNA condensates at 5 mM Mg²⁺ fused in the order of minutes (**Video S1**), and at Mg²⁺ concentrations >7 mM,
 486 gel-like morphologies were observed. Our reconstituted system approximates nucleoli and, along with recent
 487 findings of rRNA movement through the nucleolus (44), supports this hypothesis that the viscoelastic contribution
 488 of RNA in nucleoli accounts for its irregular shapes and slow fusion dynamics.

489 Additionally, our *in vitro* studies provides a valuable caveat for the interpretation of underlying causes observed in
 490 ATP depletion studies. Numerous works on ATP-depleted nucleoli, purified and *in vivo*, resulted in irregularly
 491 shaped structures reminiscent of incomplete fusion (9,11,45,46), and a similar observation of slowed recovery
 492 dynamics was observed in ATP-depleted cells containing CAG-repeat RNA condensates (47). The slowed
 493 condensate dynamics upon ATP depletion in all cases was attributed to an unknown ATP-dependent
 494 process/enzyme required to maintain condensate fluidity. However, our ATP-depleted *in vitro* model, when
 495 apyrase was added, challenges this perspective. Here, the depleted ATP liberates Mg²⁺, resulting in the morphed
 496 gel-like appearance of the protein-RNA condensates. Our results can help explain these *in vivo* observations,
 497 without the need for ATP-dependent enzymatic activity to maintain condensate fluidity, by highlighting the
 498 importance of considering free Mg²⁺ in the interpretation of ATP depletion results. Beyond enzymes, it is also
 499 valuable to consider the changes in ATP levels during a cell cycle (8,48), and how this could impact the fluidity
 500 and condensate properties of nucleoli and other protein-RNA condensates.

501 Together, our results show that protein-RNA condensates are responsive, responding to changes in the local
 502 environment: from temperature to differences in Mg²⁺ and ATP concentrations. The small molecules influenced
 503 partitioning of constituent condensate components, which in turn affected client partitioning. Transient changes to
 504 ATP levels may be how cells regulate the amount of free Mg²⁺ and thereby control the dynamics of RNA-based
 505 condensates, such as the nucleolus.

506

507 SUPPLEMENTARY DATA

508 Supplementary Data are available online.

509 FUNDING

510 This work was supported by the Netherlands Organisation for Scientific Research (NWO) through a Startup grant
 511 to E.S.

512

513 CONFLICT OF INTEREST

514 The authors have no conflict of interest.

515

516 ACKNOWLEDGEMENTS

517 We thank Prof. Richard Kriwacki (St. Jude Children's Hospital) for providing us with the NPM1-GFP plasmid, and
 518 Davin Elian for his help in cloning the NPM1-wt plasmid. Lastly, we thank Dr. Aigars Piruska (Radboud University)
 519 for his assiduous patience and microscopy technician skills.

520

521 REFERENCES

522

- 523 1. Roden, C., and A. S. Gladfelter. 2021. RNA contributions to the form and function of biomolecular condensates. *Nature*
 524 *Reviews Molecular Cell Biology*. 22(3):183-195, doi: 10.1038/s41580-020-0264-6, <https://doi.org/10.1038/s41580-020-0264-6>.
- 525 2. Guo, L., and J. Shorter. 2015. It's Raining Liquids: RNA Tunes Viscoelasticity and Dynamics of Membraneless Organelles.
 526 *Molecular Cell*. 60(2):189-192, doi: <https://doi.org/10.1016/j.molcel.2015.10.006>,
 527 <https://www.sciencedirect.com/science/article/pii/S109727651500773X>.
- 528 3. Rhine, K., V. Vidaurre, and S. Myong. 2020. RNA Droplets. *Annu Rev Biophys*. 49(1):247-265, doi: 10.1146/annurev-biophys-
 529 052118-115508, <https://www.ncbi.nlm.nih.gov/pubmed/32040349>.

- 530 4. Yamagami, R., J. P. Sieg, and P. C. Bevilacqua. 2021. Functional Roles of Chelated Magnesium Ions in RNA Folding and
531 Function. *Biochemistry*. 60(31):2374-2386, doi: 10.1021/acs.biochem.1c00012,
532 <https://www.ncbi.nlm.nih.gov/pubmed/34319696>.
- 533 5. Wright, R. H. G., F. Le Dily, and M. Beato. 2019. ATP, Mg(2+), Nuclear Phase Separation, and Genome Accessibility. *Trends in*
534 *biochemical sciences*. 44(7):565-574, doi: 10.1016/j.tibs.2019.03.001, <https://www.ncbi.nlm.nih.gov/pubmed/31072688>.
- 535 6. Nierhaus, K. H. 2014. Mg²⁺, K⁺, and the ribosome. *J Bacteriol*. 196(22):3817-3819, doi: 10.1128/JB.02297-14,
536 <https://www.ncbi.nlm.nih.gov/pubmed/25225274>.
- 537 7. Gout, E., F. Rebeille, R. Douce, and R. Bigny. 2014. Interplay of Mg²⁺, ADP, and ATP in the cytosol and mitochondria:
538 unravelling the role of Mg²⁺ in cell respiration. *Proc Natl Acad Sci U S A*. 111(43):E4560-4567, doi: 10.1073/pnas.1406251111,
539 <https://www.ncbi.nlm.nih.gov/pubmed/25313036>.
- 540 8. Maeshima, K., T. Matsuda, Y. Shindo, H. Imamura, S. Tamura, R. Imai, S. Kawakami, R. Nagashima, T. Soga, H. Noji, K. Oka, and
541 T. Nagai. 2018. A Transient Rise in Free Mg(2+) Ions Released from ATP-Mg Hydrolysis Contributes to Mitotic Chromosome
542 Condensation. *Curr Biol*. 28(3):444-451 e446, doi: 10.1016/j.cub.2017.12.035,
543 <https://www.ncbi.nlm.nih.gov/pubmed/29358072>.
- 544 9. Brangwynne, C. P., T. J. Mitchison, and A. A. Hyman. 2011. Active liquid-like behavior of nucleoli determines their size and
545 shape in *Xenopus laevis* oocytes. *Proc Natl Acad Sci U S A*. 108(11):4334-4339, doi: 10.1073/pnas.1017150108,
546 <https://www.ncbi.nlm.nih.gov/pubmed/21368180>.
- 547 10. Feric, M., N. Vaidya, T. S. Harmon, D. M. Mitrea, L. Zhu, T. M. Richardson, R. W. Kriwacki, R. V. Pappu, and C. P. Brangwynne.
548 2016. Coexisting Liquid Phases Underlie Nucleolar Subcompartments. *Cell*. 165(7):1686-1697, doi: 10.1016/j.cell.2016.04.047,
549 <https://www.ncbi.nlm.nih.gov/pubmed/27212236> (Article).
- 550 11. Caragine, C. M., S. C. Haley, and A. Zidovska. 2019. Nucleolar dynamics and interactions with nucleoplasm in living cells. *Elife*.
551 8:e47533, doi: 10.7554/eLife.47533, <https://www.ncbi.nlm.nih.gov/pubmed/31769409>.
- 552 12. Ma, W., G. Zheng, W. Xie, and C. Mayr. 2021. In vivo reconstitution finds multivalent RNA–RNA interactions as drivers of
553 mesh-like condensates. *elife*. 10:e64252, doi: 10.7554/eLife.64252, <https://doi.org/10.7554/eLife.64252>.
- 554 13. Mitrea, D. M., J. A. Cika, C. S. Guy, D. Ban, P. R. Banerjee, C. B. Stanley, A. Nourse, A. A. Deniz, and R. W. Kriwacki. 2016.
555 Nucleophosmin integrates within the nucleolus via multi-modal interactions with proteins displaying R-rich linear motifs and
556 rRNA. *Elife*. 5:e13571, doi: 10.7554/eLife.13571, <https://www.ncbi.nlm.nih.gov/pubmed/26836305>.
- 557 14. Vibhute, M. A., M. H. Schaap, R. J. M. Maas, F. H. T. Nelissen, E. Spruijt, H. A. Heus, M. M. K. Hansen, and W. T. S. Huck. 2020.
558 Transcription and Translation in Cytomimetic Protocells Perform Most Efficiently at Distinct Macromolecular Crowding
559 Conditions. *ACS Synthetic Biology*. doi: 10.1021/acssynbio.0c00330, <https://doi.org/10.1021/acssynbio.0c00330>.
- 560 15. Awwad, D. A., A. R. Rahmouni, and F. Aboul-Ela. 2020. Protocol for efficient fluorescence 3' end-labeling of native noncoding
561 RNA domains. *MethodsX*. 7:101148, doi: 10.1016/j.mex.2020.101148, <https://www.ncbi.nlm.nih.gov/pubmed/33299805>.
- 562 16. Taylor, N. O., M. T. Wei, H. A. Stone, and C. P. Brangwynne. 2019. Quantifying Dynamics in Phase-Separated Condensates
563 Using Fluorescence Recovery after Photobleaching. *Biophys J*. 117(7):1285-1300, doi: 10.1016/j.bpj.2019.08.030,
564 <https://www.ncbi.nlm.nih.gov/pubmed/31540706>.
- 565 17. Spoelstra, W. K., E. O. van der Sluis, M. Dogterom, and L. Reese. 2020. Nonspherical Coacervate Shapes in an Enzyme-Driven
566 Active System. *Langmuir*. 36(8):1956-1964, doi: 10.1021/acs.langmuir.9b02719,
567 <https://www.ncbi.nlm.nih.gov/pubmed/31995710>.
- 568 18. Kolbeck, P. J., W. Vanderlinden, G. Gemmecker, C. Gebhardt, M. Lehmann, A. Lak, T. Nicolaus, T. Cordes, and J. Lipfert. 2021.
569 Molecular structure, DNA binding mode, photophysical properties and recommendations for use of SYBR Gold. *Nucleic Acids*
570 *Research*. 49(9):5143-5158, doi: 10.1093/nar/gkab265, <https://doi.org/10.1093/nar/gkab265>.
- 571 19. Otsu, N. 1979. A Threshold Selection Method from Gray-Level Histograms. *IEEE Transactions on Systems, Man, and*
572 *Cybernetics*. 9(1):62-66, doi: 10.1109/tsmc.1979.4310076.
- 573 20. Negi, S. S., and M. O. Olson. 2006. Effects of interphase and mitotic phosphorylation on the mobility and location of nucleolar
574 protein B23. *J Cell Sci*. 119(Pt 17):3676-3685, doi: 10.1242/jcs.03090, <https://www.ncbi.nlm.nih.gov/pubmed/16912078>.
- 575 21. Guillén-Boixet, J., A. Kopach, A. S. Holehouse, S. Wittmann, M. Jahnel, R. Schlüßler, K. Kim, I. R. E. A. Trussina, J. Wang, D.
576 Mateju, I. Poser, S. Maharana, M. Ruer-Gruß, D. Richter, X. Zhang, Y.-T. Chang, J. Guck, A. Honigmann, J. Mahamid, A. A.
577 Hyman, R. V. Pappu, S. Alberti, and T. M. Franzmann. 2020. RNA-Induced Conformational Switching and Clustering of G3BP
578 Drive Stress Granule Assembly by Condensation. *Cell*. 181(2):346-361.e317, doi: <https://doi.org/10.1016/j.cell.2020.03.049>,
579 <https://www.sciencedirect.com/science/article/pii/S0092867420303421>.
- 580 22. Mours, M., and H. H. Winter. 1996. Relaxation patterns of nearly critical gels. *Macromolecules*. 29(22):7221-7229, doi: DOI
581 10.1021/ma9517097, <Go to ISI>://WOS:A1996VN88800035.
- 582 23. Suman, K., and Y. M. Joshi. 2020. On the universality of the scaling relations during sol-gel transition. *Journal of Rheology*.
583 64(4):863-877, doi: 10.1122/1.5134115, <Go to ISI>://WOS:000537740000007.
- 584 24. Boeynaems, S., A. S. Holehouse, V. Weinhardt, D. Kovacs, J. Van Lindt, C. Larabell, L. V. D. Bosch, R. Das, P. S. Tompa, R. V.
585 Pappu, and A. D. Gitler. 2019. Spontaneous driving forces give rise to protein–RNA condensates with coexisting phases and
586 complex material properties. *Proceedings of the National Academy of Sciences of the United States of America*. 116(16):7889-
587 7898, doi: 10.1073/pnas.1821038116, [https://www.scopus.com/inward/record.uri?eid=2-s2.0-
588 85064355666&doi=10.1073%2fpnas.1821038116&partnerID=40&md5=b34f496f7c723c1bc64a2b60685f7b6e](https://www.scopus.com/inward/record.uri?eid=2-s2.0-85064355666&doi=10.1073%2fpnas.1821038116&partnerID=40&md5=b34f496f7c723c1bc64a2b60685f7b6e) (Article).

- 589 25. Newby Lambert, M., E. Vocker, S. Blumberg, S. Redemann, A. Gajraj, J. C. Meiners, and N. G. Walter. 2006. Mg²⁺-induced
590 compaction of single RNA molecules monitored by tethered particle microscopy. *Biophys J.* 90(10):3672-3685, doi:
591 10.1529/biophysj.105.067793, <https://www.ncbi.nlm.nih.gov/pubmed/16500956>.
- 592 26. Carvalho-Silva, V. H., N. D. Coutinho, and V. Aquilanti. 2019. Temperature Dependence of Rate Processes Beyond Arrhenius
593 and Eyring: Activation and Transitivity. *Front Chem.* 7(380):380, doi: 10.3389/fchem.2019.00380,
594 <https://www.ncbi.nlm.nih.gov/pubmed/31192196> (Original Research).
- 595 27. Riback, J. A., L. Zhu, M. C. Ferrolino, M. Tolbert, D. M. Mitrea, D. W. Sanders, M. T. Wei, R. W. Kriwacki, and C. P. Brangwynne.
596 2020. Composition-dependent thermodynamics of intracellular phase separation. *Nature.* 581(7807):209-214, doi:
597 10.1038/s41586-020-2256-2, <https://www.ncbi.nlm.nih.gov/pubmed/32405004>.
- 598 28. Gabriel, T. E., and D. Günzel. 2007. Quantification of Mg²⁺ extrusion and cytosolic Mg²⁺-buffering in *Xenopus* oocytes.
599 *Archives of biochemistry and biophysics.* 458(1):3-15, doi: <https://doi.org/10.1016/j.abb.2006.07.007>,
600 <https://www.sciencedirect.com/science/article/pii/S0003986106002645>.
- 601 29. Romani, A. M. P. 2011. Intracellular magnesium homeostasis. In *Magnesium in the Central Nervous System.* pp. 13-58.
- 602 30. Chang, J. H., J. Y. Lin, M. H. Wu, and B. Y. Yung. 1998. Evidence for the ability of nucleophosmin/B23 to bind ATP. *Biochem J.*
603 329 (Pt 3)(3):539-544, doi: 10.1042/bj3290539, <https://www.ncbi.nlm.nih.gov/pubmed/9445380>.
- 604 31. Choi, J. W., S. B. Lee, J. Y. Ahn, and K. H. Lee. 2008. Disruption of ATP binding destabilizes NPM/B23 and inhibits anti-apoptotic
605 function. *Journal of Biochemistry and Molecular Biology.* 41(12):840-845, doi: 10.5483/bmbrep.2008.41.12.840,
606 [https://www.scopus.com/inward/record.uri?eid=2-s2.0-
607 58149352992&doi=10.5483%2fbmbrep.2008.41.12.840&partnerID=40&md5=c58975cab0b978e2da5144bd7d65ecd1](https://www.scopus.com/inward/record.uri?eid=2-s2.0-58149352992&doi=10.5483%2fbmbrep.2008.41.12.840&partnerID=40&md5=c58975cab0b978e2da5144bd7d65ecd1)
608 (Article).
- 609 32. Wang, D., A. Baumann, A. Szebeni, and M. O. Olson. 1994. The nucleic acid binding activity of nucleolar protein B23.1 resides
610 in its carboxyl-terminal end. *Journal of Biological Chemistry.* 269(49):30994-30998, doi: 10.1016/S0021-9258(18)47380-2,
611 [https://doi.org/10.1016/S0021-9258\(18\)47380-2](https://doi.org/10.1016/S0021-9258(18)47380-2).
- 612 33. Musinova, Y. R., E. Y. Kananykhina, D. M. Potashnikova, O. M. Lisitsyna, and E. V. Sheval. 2015. A charge-dependent
613 mechanism is responsible for the dynamic accumulation of proteins inside nucleoli. *Biochimica et biophysica acta.*
614 1853(1):101-110, doi: 10.1016/j.bbamcr.2014.10.007, <https://www.ncbi.nlm.nih.gov/pubmed/25315210>.
- 615 34. Nachmani, D., A. H. Bothmer, S. Grisendi, A. Mele, D. Bothmer, J. D. Lee, E. Monteleone, K. Cheng, Y. Zhang, A. C. Bester, A.
616 Guzzetti, C. A. Mitchell, L. M. Mendez, O. Pozdnyakova, P. Sportoletti, M. P. Martelli, T. J. Vulliamy, M. Safra, S. Schwartz, L.
617 Luzzatto, O. Bluteau, J. Soulier, R. B. Darnell, B. Falini, I. Dokal, K. Ito, J. G. Clohessy, and P. P. Pandolfi. 2019. Germline NPM1
618 mutations lead to altered rRNA 2'-O-methylation and cause dyskeratosis congenita. *Nat Genet.* 51(10):1518-1529, doi:
619 10.1038/s41588-019-0502-z, <https://www.ncbi.nlm.nih.gov/pubmed/31570891>.
- 620 35. Yamamoto, T., Y. Shimizu, T. Ueda, and Y. Shiro. 2010. Mg²⁺ dependence of 70 S ribosomal protein flexibility revealed by
621 hydrogen/deuterium exchange and mass spectrometry. *The Journal of biological chemistry.* 285(8):5646-5652, doi:
622 10.1074/jbc.M109.081836, <https://www.ncbi.nlm.nih.gov/pubmed/20022945>.
- 623 36. Okuwaki, M., S. Saito, H. Hirawake-Mogi, and K. Nagata. 2021. The interaction between nucleophosmin/NPM1 and the large
624 ribosomal subunit precursors contribute to maintaining the nucleolar structure. *Biochim Biophys Acta Mol Cell Res.*
625 1868(1):118879, doi: 10.1016/j.bbamcr.2020.118879, <https://www.ncbi.nlm.nih.gov/pubmed/33039556>.
- 626 37. Alshareedah, I., G. M. Thurston, and P. R. Banerjee. 2021. Quantifying viscosity and surface tension of multicomponent
627 protein-nucleic acid condensates. *Biophys J.* doi: 10.1016/j.bpj.2021.01.005,
628 <https://www.ncbi.nlm.nih.gov/pubmed/33453268>.
- 629 38. Iglesias-Artola, J. M., B. Drobot, M. Kar, A. W. Fritsch, H. Mutschler, T. Y. Dora Tang, and M. Kreysing. 2022. Charge-density
630 reduction promotes ribozyme activity in RNA-peptide coacervates via RNA fluidization and magnesium partitioning. *Nature*
631 *Chemistry.* doi: 10.1038/s41557-022-00890-8, <https://doi.org/10.1038/s41557-022-00890-8>.
- 632 39. Zhu, L., T. M. Richardson, L. Wacheul, M. T. Wei, M. Feric, G. Whitney, D. L. J. Lafontaine, and C. P. Brangwynne. 2019.
633 Controlling the material properties and rRNA processing function of the nucleolus using light. *Proc Natl Acad Sci U S A.*
634 116(35):17330-17335, doi: 10.1073/pnas.1903870116, <https://www.ncbi.nlm.nih.gov/pubmed/31399547> (Article).
- 635 40. Jawerth, L., E. Fischer-Friedrich, S. Saha, J. Wang, T. Franzmann, X. Zhang, J. Sachweh, M. Ruer, M. Ijavi, S. Saha, J. Mahamid,
636 A. A. Hyman, and F. Jülicher. 2020. Protein condensates as aging Maxwell fluids. *Science.* 370(6522):1317-1323, doi:
637 10.1126/science.aaw4951, <https://science.sciencemag.org/content/sci/370/6522/1317.full.pdf>.
- 638 41. Hong, K., D. Song, and Y. Jung. 2020. Behavior control of membrane-less protein liquid condensates with metal ion-induced
639 phase separation. *Nature Communications.* 11(1):5554, doi: 10.1038/s41467-020-19391-8, [https://doi.org/10.1038/s41467-
640 020-19391-8](https://doi.org/10.1038/s41467-020-19391-8).
- 641 42. Latonen, L. 2019. Phase-to-Phase With Nucleoli - Stress Responses, Protein Aggregation and Novel Roles of RNA. *Front Cell*
642 *Neurosci.* 13(151):151, doi: 10.3389/fncel.2019.00151, <https://www.ncbi.nlm.nih.gov/pubmed/31080406> (Review).
- 643 43. Okuwaki, M., A. Sumi, M. Hisaoka, A. Saotome-Nakamura, S. Akashi, Y. Nishimura, and K. Nagata. 2012. Function of homo- and
644 hetero-oligomers of human nucleoplasmin/nucleophosmin family proteins NPM1, NPM2 and NPM3 during sperm chromatin
645 remodeling. *Nucleic Acids Res.* 40(11):4861-4878, doi: 10.1093/nar/gks162,
646 <https://www.ncbi.nlm.nih.gov/pubmed/22362753>.
- 647 44. Riback, J. A., J. M. Eeftens, D. S. Lee, S. A. Quinodoz, L. Beckers, L. A. Becker, and C. P. Brangwynne. 2022. Viscoelastic RNA
648 entanglement and advective flow underlies nucleolar form and function. *Biophysical Journal.* 121(3):473a-473a, doi:
649 10.1101/2021.12.31.474660, [Go to ISI>://WOS:000759523003117](https://doi.org/10.1101/2021.12.31.474660).

- 650 45. Hayes, M. H., E. H. Peuchen, N. J. Dovichi, and D. L. Weeks. 2018. Dual roles for ATP in the regulation of phase separated
651 protein aggregates in *Xenopus* oocyte nucleoli. *eLife*. 7:e35224, doi: 10.7554/eLife.35224,
652 <https://doi.org/10.7554/eLife.35224>.
- 653 46. Park, H., S. S. Han, Y. Sako, and C. G. Pack. 2015. Dynamic and unique nucleolar microenvironment revealed by fluorescence
654 correlation spectroscopy. *FASEB Journal*. 29(3):837-848, doi: 10.1096/fj.14-254110,
655 [https://www.scopus.com/inward/record.uri?eid=2-s2.0-84937421464&doi=10.1096%2ffj.14-
656 254110&partnerID=40&md5=43633d4481b03315edca2690e8dbab66](https://www.scopus.com/inward/record.uri?eid=2-s2.0-84937421464&doi=10.1096%2ffj.14-254110&partnerID=40&md5=43633d4481b03315edca2690e8dbab66) (Article).
- 657 47. Jain, A., and R. D. Vale. 2017. RNA phase transitions in repeat expansion disorders. *Nature*. 546(7657):243-247, doi:
658 10.1038/nature22386, <https://www.ncbi.nlm.nih.gov/pubmed/28562589>.
- 659 48. Kang, J. H., G. Katsikis, Z. Li, K. M. Sapp, M. A. Stockslager, D. Lim, M. G. Vander Heiden, M. B. Yaffe, S. R. Manalis, and T. P.
660 Miettinen. 2020. Monitoring and modeling of lymphocytic leukemia cell bioenergetics reveals decreased ATP synthesis during
661 cell division. *Nature Communications*. 11(1):4983, doi: 10.1038/s41467-020-18769-y, [https://doi.org/10.1038/s41467-020-
662 18769-y](https://doi.org/10.1038/s41467-020-18769-y).

663
664

Journal Pre-proof

665 **TABLE AND FIGURE LEGENDS**

666

667 **Figure 1.** Mg²⁺-induced RNA compaction leads to slow dynamics and gelation. (A) NPM1 protein and rRNA, both
 668 labelled with different fluorophores, are mixed together to form condensates that show differences in FRAP
 669 recovery (B & C), where NPM1 (green) recovers faster than rRNA (red). (D) The recovery of rRNA slows to a halt
 670 at Mg²⁺ ion concentrations > 7 mM (shaded in yellow) and shows critical scaling behavior (purple fitted line)
 671 indicating it forms a gel, whereas the NPM1 protein remains mobile. (E) The decrease in percentage recovery for
 672 both NPM1 and rRNA reflects the gel environment at higher Mg²⁺ concentrations. (F) These droplets become gels
 673 at higher Mg²⁺ where the rRNA is fully arrested, indicated by bleached regions not recovering (white arrows). In
 674 order to test the RNA compaction hypothesis, NPM1-rRNA condensate morphology (G) and FRAP recovery
 675 parameters (H & I) were compared with NPM1-pA and NPM1-pU condensates. The errors in this figure are
 676 standard deviations from triplicate measurements. Scale bars are all 10 μm.

677

678 **Figure 2.** Temperature and ATP can reverse the effect of Mg²⁺-induced RNA condensation. (A) NPM1-rRNA
 679 condensates aging at 20 °C with individual τ for rRNA measured over time (dots) and a fitted exponential curve
 680 (line). (B) The extracted plateau τ at maturation for rRNA (red) and NPM1 (green) was plotted for aged droplets at
 681 different temperatures in 0 mM Mg²⁺ buffer. The errors here are derived from the exponential fits. (C) Forming
 682 NPM1-rRNA condensates at 8 °C in buffer containing magnesium resulted in irregular gel-like morphologies that
 683 changed to spherical droplets at increasing temperatures, with increased circularities. (D) The gels formed in 14
 684 mM Mg²⁺ buffer also liquefied after 11 mM ATP addition, with increasing circularity reflected in the changed
 685 morphology of the NPM1-rRNA condensates. (E) The FRAP recovery over times for samples that contain ATP
 686 (yellow), ADP (orange) or AMP (blue) compared with just the 5 mM Mg²⁺ buffer (grey). The extracted τ (F) and
 687 percentage recoveries (G) indicate that the better Mg²⁺-chelating ability of ATP compared to other adenosine
 688 nucleotides caused the condensates to liquefy. The errors in figures E-G are standard deviations from at least
 689 duplicate measurements. Scale bars are all 10 μm.

690

691 **Figure 3:** The effect of Mg²⁺ and ATP on partitioning of components, clients and 70S ribosomes. The partitioning
 692 coefficients of rRNA (A) and NPM1 (B) at different Mg²⁺ and ATP concentrations. (C) The partitioning coefficients
 693 of 5,6-FAM-RP3 peptide (blue) and 5,6-FAM-SNORD52 RNA (orange) at different ATP concentrations in a 5 mM
 694 Mg²⁺ base buffer. Confocal microscope images of NPM1-rRNA condensates with 70S ribosome as the client (D &
 695 E). (D) The images show that rRNA-A647 is excluded from the ribosome fluorescence, whereas (E) shows NPM1-
 696 A488 fluorescence as spherical droplets that occupy both locations where there is 70S ribosome and rRNA. (F)
 697 The formation of the ribosome halo over time as indicated by an increase in fluorescence pixel intensity as peaks
 698 at the edges of the droplet. The errors in this figure are standard deviations from triplicate measurements. Scale
 699 bars are all 10 μm.

700

701 **Figure 4:** Enzymatic control of ATP concentrations influences condensate morphology and dynamics. (A) Apyrase
 702 enzymes catalyze the removal of phosphate groups from ATP to form AMP, a nucleotide that poorly chelates Mg²⁺.
 703 (B) The effect of apyrase on the dynamics of rRNA after FRAP is clearly shown (B-D) where rRNA recovery in the
 704 presence of ATP (yellow) drops when apyrase (purple) is added. In fact, the resulting FRAP parameters (C & D)
 705 show that apyrase converts ATP to AMP which imbues the rRNA with gel-like dynamics. The errors in this figure
 706 are standard deviations from triplicate measurements. The morphology of NPM1-rRNA condensates at 18 °C in 5
 707 mM Mg²⁺ buffer (E) with 5 mM ATP added (F), and when apyrase is also added (G) shows the changes in
 708 morphology that is expected from gel-like condensates in buffer containing Mg²⁺ that stabilizes RNA-RNA
 709 interactions, and spherical morphology in conditions where ATP chelates the Mg²⁺ and liquefies these interactions.
 710 (H) This series of confocal images over time of labelled 70S ribosomes show the disappearance of the ribosome
 711 halo and puncta, as apyrase was added. ATP depletion results in higher Mg²⁺, which stabilizes the ribosomes and
 712 causes them to dissipate back into the dilute phase. Scale bars are all 10 μm.

